nature energy

ARTICLES

PUBLISHED: 21 MARCH 2016 | ARTICLE NUMBER: 16030 | DOI: 10.1038/NENERGY.2016.30

High-power all-solid-state batteries using sulfide superionic conductors

Yuki Kato[1,2,3*†], Satoshi Hori[2†], Toshiya Saito[1], Kota Suzuki[2], Masaaki Hirayama[2], Akio Mitsui[4], Masao Yonemura[5], Hideki Iba[1] and Ryoji Kanno[2*]

Compared with lithium-ion batteries with liquid electrolytes, all-solid-state batteries offer an attractive option owing to their potential in improving the safety and achieving both high power and high energy densities. Despite extensive research efforts, the development of all-solid-state batteries still falls short of expectation largely because of the lack of suitable candidate materials for the electrolyte required for practical applications. Here we report lithium superionic conductors with an exceptionally high conductivity (25 mS cm^{-1} for $Li_{9.54}Si_{1.74}P_{1.44}S_{11.7}Cl_{0.3}$), as well as high stability (~0 V versus Li metal for $Li_{9.6}P_3S_{12}$). A fabricated all-solid-state cell based on this lithium conductor is found to have very small internal resistance, especially at 100 °C. The cell possesses high specific power that is superior to that of conventional cells with liquid electrolytes. Stable cycling with a high current density of 18 C (charging/discharging in just three minutes; where C is the C-rate) is also demonstrated.

So far, batteries and capacitors have generally been powered by liquid electrolytes[1,2]. However, owing to some intrinsic characteristics of liquid electrolytes (for example, low lithium transport number, complex reaction at the solid/liquid interface, and thermal instability), it has not been possible to simultaneously achieve high energy and power in any of the current electrochemical devices[2–5]. Therefore, the all-solid-state battery has been proposed and researched as a potential candidate among various electrochemical energy storage devices for achieving both high energy and high power densities[6]. Moreover, the solidification of the electrolyte provides an additional advantage for use in battery applications. In the case of the all-solid-battery system, the non-liquid nature of the electrolyte allows stacking of the battery cells in a single package without ionic short circuit. Such a battery configuration decreases the dead space between single cells, as shown in Supplementary Fig. 1 (see also Supplementary Video). In addition, this structure is suitable for applications requiring a high voltage and limited space, such as vehicle power sources. However, despite the expected advantages of all-solid-state batteries, their power characteristics and energy densities must be improved to allow their application in technologies such as long-range electric vehicles.

All-solid-state batteries contain a cathode, anode and electrolyte, and the properties of the batteries depend mostly on the characteristics of the electrolyte. The low rate capabilities and low energy densities of the all-solid-state batteries are partly due to a lack of suitable electrolyte materials that exhibit high ionic conductivity comparable to liquid electrolytes. Recently, $Li_7P_3S_{11}$ (ref. 7) and LGPS ($Li_{10}GeP_2S_{12}$; ref. 8), which are ionic conducting materials, were discovered. These materials have a body-centred cubic anion sub-lattice structure[9] and exhibit higher ionic conductivity than liquid electrolytes. However, the former has issues with chemical stability[10], and the latter contains the expensive element germanium. Thus, at present, no candidate material exists for an actual battery device. In addition, the potential advantages of all-solid-state batteries have not yet been realized with cells

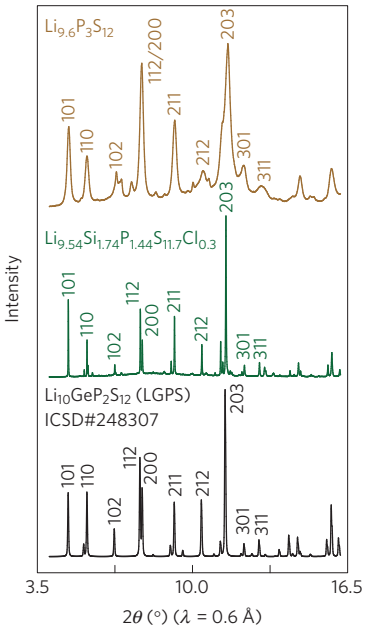

Figure 1 | X-ray diffraction patterns of the LGPS family. Synchrotron X-ray diffraction patterns of $Li_{9.6}P_3S_{12}$ (upper), $Li_{9.54}Si_{1.74}P_{1.44}S_{11.7}Cl_{0.3}$ (middle), and $Li_{10}GeP_2S_{12}$ (lower). All of the patterns were indexed to the same space group, $P4_2/nmc$ (137).

[1]Battery Research Division, Higashifuji Technical Center, Toyota Motor Corporation, 1200 Mishuku, Susono, Shizuoka 410-1193, Japan. [2]Department of Electronic Chemistry, Interdisciplinary Graduate School of Science and Engineering, Tokyo Institute of Technology, 4259 Nagatsuta, Midori, Yokohama 226-8502, Japan. [3]Battery AT, Advanced Technology 1, Toyota Motor Europe NV/SA, Hoge Wei 33A B-1930, Zaventem, Belgium. [4]Material analysis Department, Material Engineering Division, Toyota Motor Corporation, 1 Toyota-cho, Toyota, Aichi 471-8572, Japan. [5]Institute of Materials Structure Science (IMSS), High Energy Accelerator Research Organization (KEK), Shirakata, Tokai, Ibaraki 319-1106, Japan. †These authors contributed equally to this work. *e-mail: yuki.katoh@toyota-europe.com; kanno@echem.titech.ac.jp

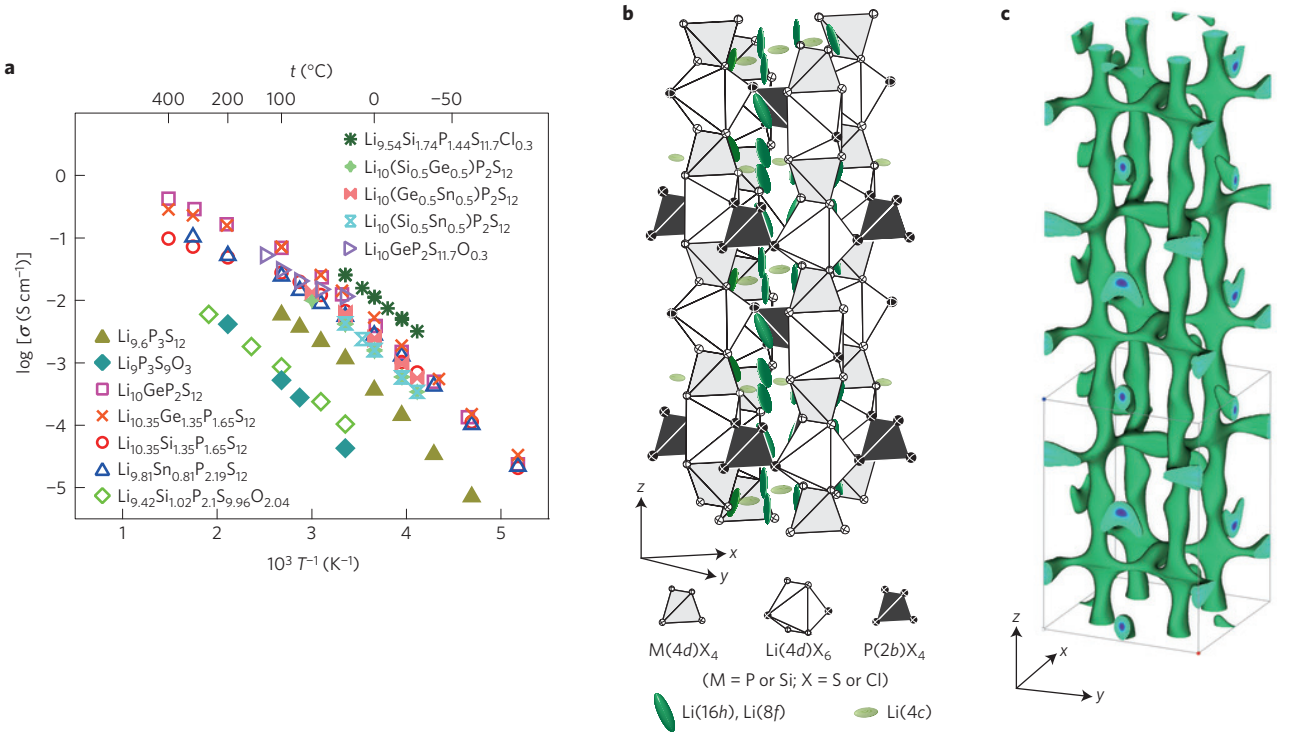

Figure 2 | Ionic conductivity and crystal structure of $Li_{9.54}Si_{1.74}P_{1.44}S_{11.7}Cl_{0.3}$. a, Arrhenius conductivity plots for the LGPS family and $Li_{9.6}P_3S_{12}$ and $Li_{9.54}Si_{1.74}P_{1.44}S_{11.7}Cl_{0.3}$, which were used as electrolytes in this study. **b**, Crystal structure of $Li_{9.54}Si_{1.74}P_{1.44}S_{11.7}Cl_{0.3}$. The thermal ellipsoids are drawn with a 50% probability. The framework structure consists of 1D polyhedral chains (edge-sharing M(4*d*)X_4 and Li(4*d*)X_6) connected by P(2*b*)X_4 tetrahedra. Conducting lithium is located on the interstitial site of Li(16*h*), Li(8*f*) and Li(4*c*). **c**, Nuclear distributions of Li atoms in $Li_{9.54}Si_{1.74}P_{1.44}S_{11.7}Cl_{0.3}$ at 25 °C, calculated using the maximum entropy method at the iso-surface level of −0.06 fm Å^{-3}.

using electrolytes available at present. Therefore, it is expected that electrolytes exhibiting high ionic conductivity and good electrochemical stability will provide a suitable electrochemical interface when combined with suitable electrodes, and allow high current capability with high charge and discharge reversibility.

In the present study, we discovered that lithium superionic conductors, $Li_{9.54}Si_{1.74}P_{1.44}S_{11.7}Cl_{0.3}$ and $Li_{9.6}P_3S_{12}$, showed the highest ionic conductivity reported for lithium conductivity, and high electrochemical stability versus lithium metal. These materials enabled the development of all-solid-state cells with extremely desirable electrochemical characteristics and demonstrated the advantages expected from all-solid-state devices.

Characteristics of superionic conductors

Both $Li_{9.54}Si_{1.74}P_{1.44}S_{11.7}Cl_{0.3}$ and $Li_{9.6}P_3S_{12}$ were confirmed to have the LGPS-type crystal structure[8] by X-ray diffraction patterns (Fig. 1) and the neutron Rietveld refinement technique (Supplementary Figs 2 and 3). The structural parameters are listed in Supplementary Tables 1 and 2. Their ionic conductivity is summarized in Fig. 2a, along with the values reported for previous LGPS electrolytes. These conductivity data are also summarized in Supplementary Table 3. The highest conductivity value obtained at room temperature for the chlorine-doped silicon-based system (25 mS cm^{-1}, $Li_{9.54}Si_{1.74}P_{1.44}S_{11.7}Cl_{0.3}$) was twice that of the original LGPS (ref. 8) and is the highest value reported so far for lithium superionic conductors. The anisotropic thermal displacement of lithium (Fig. 2b) and nuclear density distribution (Fig. 2c) indicate the three-dimensional (3D) conduction pathways (1D along the *c* axis + 2D in the *ab* plane) in $Li_{9.54}Si_{1.74}P_{1.44}S_{11.7}Cl_{0.3}$. The 1D pathway is a unique characteristic in the LGPS family[8,11,12]. However, the 2D conduction mode has not yet been experimentally observed at room temperature (only reported at 750 K (ref. 11)), despite its expected contribution towards increasing the ionic conductivity[11,12]. Therefore, this is the first example of widely distributed 3D conduction pathways in the LGPS-type structure at 25 °C, which leads to the highest ionic conductivity. Such lithium distribution might be induced by the small amount of chlorine mainly located in the unique Cl(1)(8*g*) sites, present in the P(2*b*)X_4 tetrahedra.

We also report the material $Li_{9.6}P_3S_{12}$, which has an LGPS structure and exhibits high electrochemical stability. Figure 3 shows the electrochemical stability of this material towards lithium metal, which was examined using charge and discharge data obtained from the Li/solid electrolyte/$LiCoO_2$ cells[13]. The initial efficiency of the charge/discharge cycle is an indication of the stability of the electrolyte, as lithium reacts with the electrolyte at the electrode/electrolyte interface during the first charge cycle[13]. $Li_{9.6}P_3S_{12}$ exhibited an excellent efficiency of 90%, as calculated from the discharge/charge capacity ratio and efficiency was improved during cycling (see Supplementary Fig. 4). This indicates that almost all of the lithium from the cathode was deposited as metallic lithium during charging. In contrast, the original LGPS showed a lower efficiency of 61%, indicating that a significant quantity of lithium was consumed during the reaction, generating an interfacial layer at the LGPS/lithium anode interface.

These superionic conductors were developed on the basis of synthesis strategies that are different from those used previously for the LGPS-type materials (for example, Si and Sn systems), which were based on the simple substitution of constituent elements[14–16]. To improve conductivity and electrochemical stability, our strategy is based on double substitution with aliovalent-ion doping, similar to that used for the Si–Cl system, as well as a complete material search on the simple ternary Li–P–S system. These materials were developed and purified using both compositional and reaction process optimization, and may indicate a new direction for the discovery of new materials for superionic conductors.

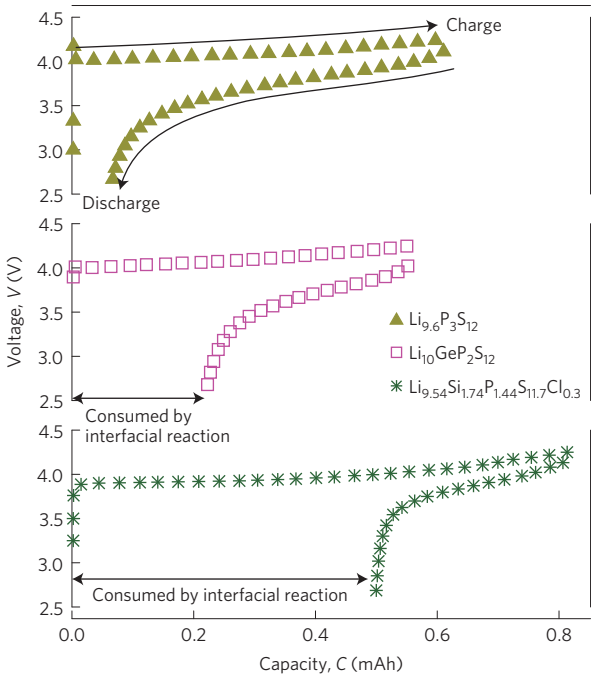

Figure 3 | Electrochemical stability of the LGPS family. Electrochemical stabilities of the electrolytes with the LGPS-type structure, characterized by the $LiCoO_2$/solid electrolyte/Li cell. Coulombic efficiency, η, was calculated as η = (discharge capacity)/(charge capacity) × 100. η for the $Li_{9.6}P_3S_{12}$, $Li_{10}GeP_2S_{12}$ and $Li_{9.54}Si_{1.74}P_{1.44}S_{11.7}Cl_{0.3}$ cells was 90%, 61% and 39%, respectively. The consumed capacity during the first charge–discharge process indicates the occurrence of side reactions leading to the generation of the surface layer.

Fabrication and performance of all-solid-state cells

Using these developed superionic conductors, we constructed two types of cell, namely high-voltage and large-current-type cells. A schematic drawing of the all-solid-state cell constructed herein is shown in Supplementary Fig. 5. The high-voltage cell required a wide operating potential to improve the capacity. The graphite anode, which has a potential of 0–0.5 V versus Li, resulted in a higher cell voltage. Lithium titanium oxide, $Li_4Ti_5O_{12}$, was used as the anode in the large-current-type cells. The selection of a suitable electrolyte in the electrode composite is key to improving the overall cell characteristics, and the best combinations of cathode composite, anode composite, and separator are summarized in Supplementary Table 4 along with the internal resistances (Supplementary Fig. 6) and specific energies of the corresponding cells. The high-voltage-type cell required an electrolyte with a wide operating potential, and therefore, $Li_{9.6}P_3S_{12}$, which has a high stability of ~0 V versus Li, was used as the anode composite. In contrast, the large-current system required an electrolyte with high ionic conductivity, and therefore, $Li_{9.54}Si_{1.74}P_{1.44}S_{11.7}Cl_{0.3}$, which has the best ionic conductivity of those tested, was employed.

Charge and discharge experiments were carried out at various current rates for both types of cell, that is, for a cell with the original LGPS system, and for the lithium-ion cell prepared herein (Supplementary Fig. 7). The charge and discharge rates of a battery are scaled by the C-rate, at which a battery is (dis)charged relative to its maximum capacity. The C-rate is determined as follows: rate nC means that the current will (dis)charge the full capacity in $1/n$ hour. The all-solid-state cells exhibited superior performance compared with the lithium-ion cells between −30 and 100 °C. In addition, the performance of the all-solid-state cells was further improved on using the present solid electrolytes. The all-solid-state cells exhibited excellent rate capabilities, with discharge current densities of 150 C at 25 °C and 1,500 C at 100 °C, as shown in Fig. 4a. The all-solid-state cells exhibited excellent cyclability over 30 cycles under a current density of 0.1 C at 25 °C (Fig. 4b). The absence of elemental diffusion and little increase in the interfacial resistance after cycling were indicators of the good chemical stability of $Li_{9.54}Si_{1.74}P_{1.44}S_{11.7}Cl_{0.3}$ (Supplementary Fig. 8). At 100 °C, the all-solid-state system also showed excellent cycling performance, with a high charge–discharge current density of 18 C (charge/discharge times of 3 min, see Fig. 4c,d). Conventional lithium-ion cells cannot operate at this temperature, owing to the thermal instability of the liquid electrolytes. The shape change in the charge–discharge curve during the cycling test is attributed to the decreased crystallinity of $LiCoO_2$ (refs 17,18), owing to the extreme cycling conditions. We determined that the all-solid-state cells exhibited excellent cycling performance, with ~75% of the first discharge capacity remaining after over 500 cycles, and a Coulombic efficiency of 100% as shown in Fig. 4e,f.

Advantage of all-solid-state configuration

Furthermore, the advantage of the all-solid-state configuration is directly evident on comparing its performance with that of a lithium-ion cell employing a liquid electrolyte. The lithium-ion cell was carefully fabricated to have the same configuration as the all-solid-state cells (Supplementary Fig. 9), to observe the effect of the state of the electrolyte (liquid or solid). Supplementary Fig. 7g shows the high rate characteristics of the lithium-ion cell prepared herein at 25 °C. The capacity of the lithium-ion cell decreased rapidly at a current density of 40 mA cm^{-2} (60 C), despite having nearly the same resistance as the all-solid-state cell (see Supplementary Fig. 10 and Supplementary Table 5) at 25 °C. At this current, the capacity of the all-solid-state cell was 75–85.4 mAh g^{-1}, which is ~3 times higher than that of the lithium-ion cell. The chronoamperometric study (Fig. 5) clearly indicates that a diffusion limitation phenomenon occurred in the lithium-ion cell at 25 °C as shown by the straight line passing through the origin in the Cottrell plot[19] (Fig. 5a) and the voltage-independent transient current[20] (Fig. 5b). At high currents, a concentration gradient is produced in the lithium-ion cell, owing to the low diffusion rates of both the anions and cations of the electrolyte salts in the solution. In contrast, the all-solid-state cell does not show such diffusion limitation behaviour. There are two possible reasons that may explain this observation: the lithium-ion concentration of ~35 mol dm^{-3} in the LGPS-type material is much higher than the 1–2 mol dm^{-3} lithium-ion concentration used in a typical liquid electrolyte; and the ionic transport number (t ~ 1.0) of the solid electrolyte is higher than that of the liquid electrolyte (t < about 0.5; ref. 21), which causes continuous and high lithium-ion diffusion even at high current drain. Interestingly, the all-solid-state cell exhibited superior properties at −30 °C, as shown in Supplementary Fig. 7h. The impedance analysis shown in Supplementary Fig. 11 indicates a large interfacial resistance in the lithium-ion cell at low temperatures caused by the de-solvation step at the liquid/solid interface[22,23]. In contrast, such a reaction did not take place at the solid/solid interface, which caused low charge transfer resistance. These results indicate the advantage of fast electrochemical reactions in the all-solid-state configuration.

An examination of Ragone plots showing the energy density versus rate property relationships provides a good indication of the performance of energy storage devices. Figure 6 shows the Ragone plots for the various electrochemical devices examined herein. Specific energy and power are plotted on the basis of the mass of the cathode active material and it allows us to evaluate the capability of the active materials in each electrochemical system. In general, the specific power is inversely related to the specific energy in electrochemical systems as shown in Fig. 6. However, the specific power of $LiNbO_3$-coated $LiCoO_2$ in the all-solid-state cells

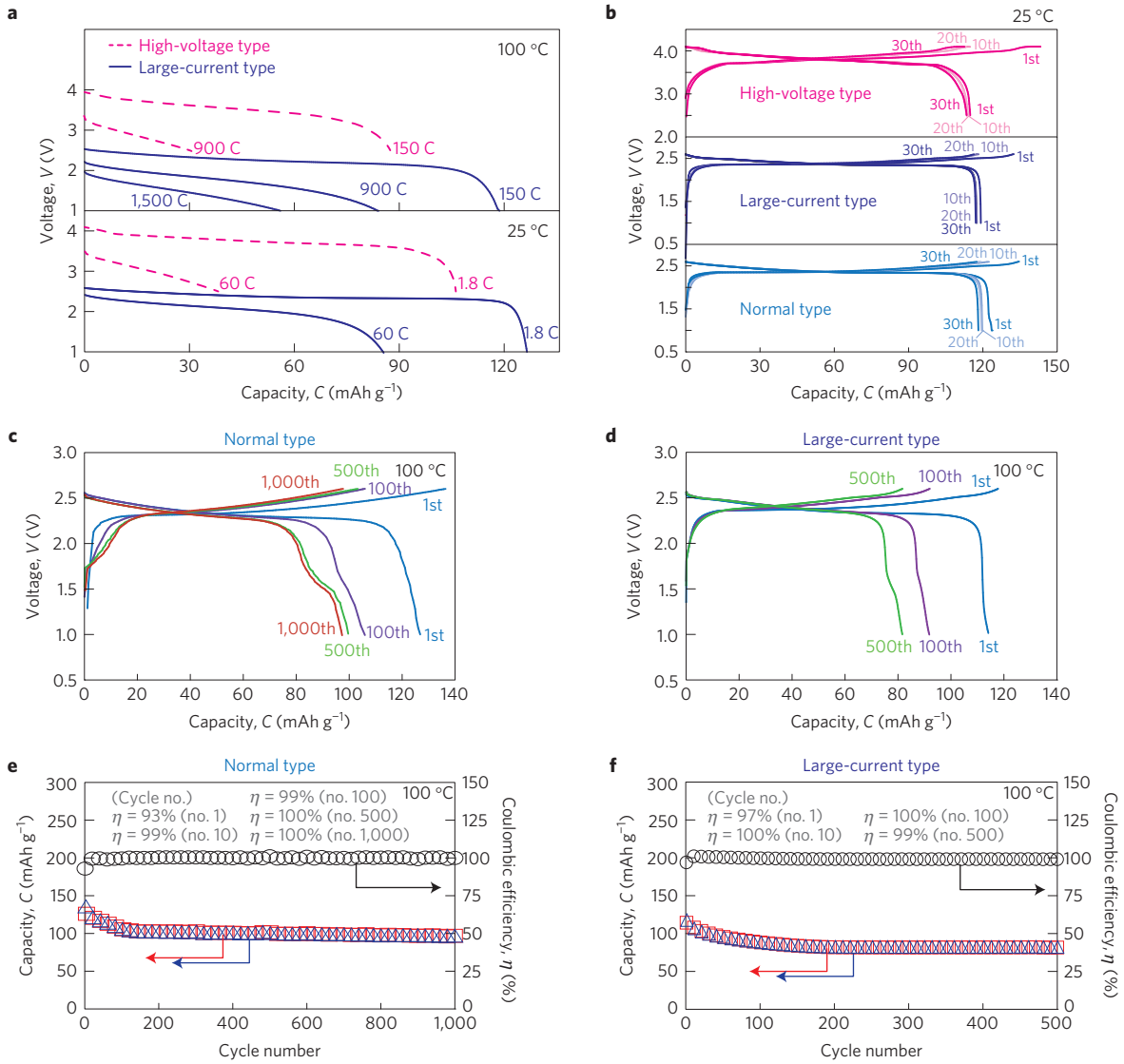

Figure 4 | Performance of the all-solid-state cells. a, Extraction of discharge curves for the prepared all-solid-state energy devices. The rate *n*C corresponds to the full charge and discharge of the theoretical capacity of 0.667 mAh in 1/*n* h. **b**, Charge–discharge profiles for all-solid-state cells at a rate of 0.1 C at 25 °C. **c**,**d**, Cycling characteristics of the charge–discharge curves for the all-solid-state cell of the normal-type cell and the large-current-type cell, respectively at 100 °C (current density = 18 C). **e**,**f**, Cycling characteristics for charge–discharge capacity and efficiency for the all-solid-state cell of the normal-type cell and the large-current-type cell, respectively. The current density of 18 C corresponds to the charging and discharging time of ~3 min (~80% theoretical capacity). Circle, efficiency; triangle, charging capacitance; square, discharging capacitance. The specific capacity was calculated on the basis of the weight of $LiNbO_3$-coated $LiCoO_2$.

was much higher than that of the lithium-ion cell, and was even higher than those of materials used for supercapacitors. As a result, the capacity versus rate curves of the present all-solid-state cells are situated in the upper right area ($E > 100$ Wh kg^{-1}, $P > 10$ kW kg^{-1}), which has not been achieved for either conventional systems (lithium-ion batteries and supercapacitors) or advanced batteries (Li–O_2, Li–S, and multivalent cation systems)[24–34].

In addition, the possibility of further improving the energy of the all-solid-state cell is shown in Supplementary Fig. 12. The all-solid-state cells exhibit good rate capability even in the high energy density configuration (high active material content or ultrathick electrode configuration; see Supplementary Table 6), indicating the large capability of all-solid-state cells for actual device application.

Conclusions

The all-solid-state cells were fabricated on the basis of the new solid electrolytes, $Li_{9.54}Si_{1.74}P_{1.44}S_{11.7}Cl_{0.3}$ and $Li_{9.6}P_3S_{12}$, which exhibit excellent ionic conductivity and electrochemical stability. These provided high power density, and ultrafast charging. The cell also exhibited improved stability and longer life compared with cells with liquid electrolyte systems under extreme cell operation conditions. These results clearly originate from the intrinsic nature of the new solid electrolytes, indicating the advantages of the all-solid-state devices over conventional electrochemical devices. In addition, possibilities exist for increasing the capability of the solid-state configuration system by using high-energy cathodic and anodic materials (for example, Li–S system), applying interfacial control techniques[13,35], and effectively utilizing the nano size effects of solids[1,3,36]. Although several technological issues still need to be addressed, including the development of a processing technology using sheeting and multiple stacking, the all-solid-state batteries can be considered a future category of electrochemical devices. These are, thus, promising candidates for energy storage devices.

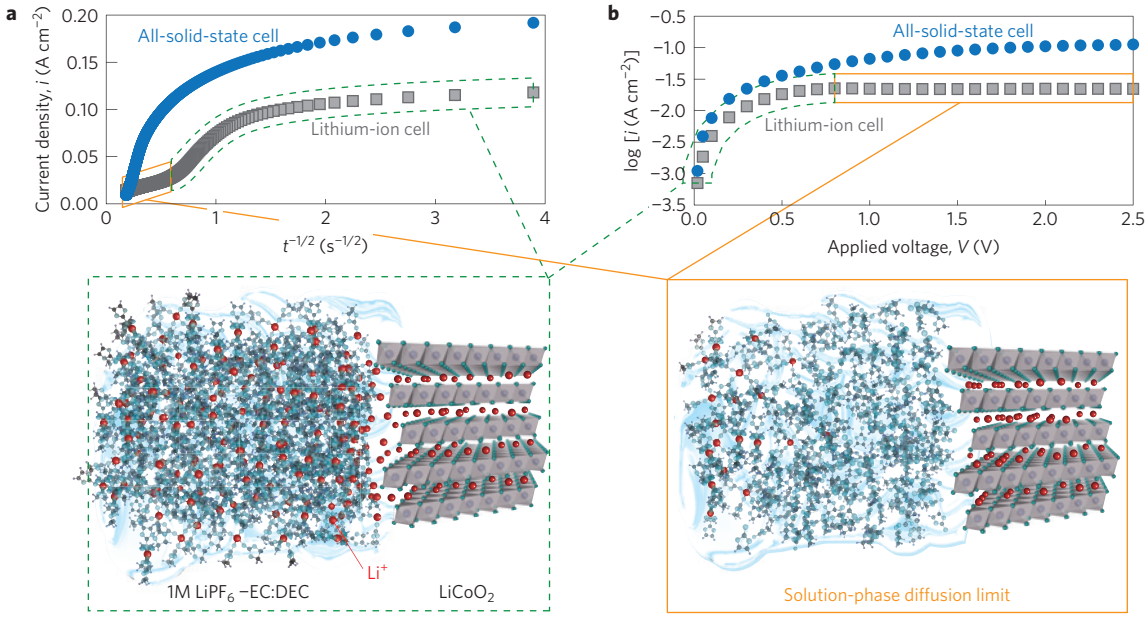

Figure 5 | Chronoamperometric behaviours of the all-solid-state and lithium-ion cells. a, Cottrell plots of the chronoamperometric curves observed with a voltage step of 1.5 V. A straight line plot is observed only for the lithium-ion cell at $t > 3$ s; the limiting current condition is satisfied only for the lithium-ion cell. **b**, Transient currents after 5 s of voltage step plotted as a function of applied voltage. The current for the lithium-ion cell remains constant for voltage steps larger than 0.8 V, which indicates diffusion limitation only for the lithium-ion cell. Insets show the cation distributions for the lithium-ion cell for non-diffusion limitation (left) and diffusion limitation (right). Almost no lithium is expected at the interface region under the diffusion-limiting conditions.

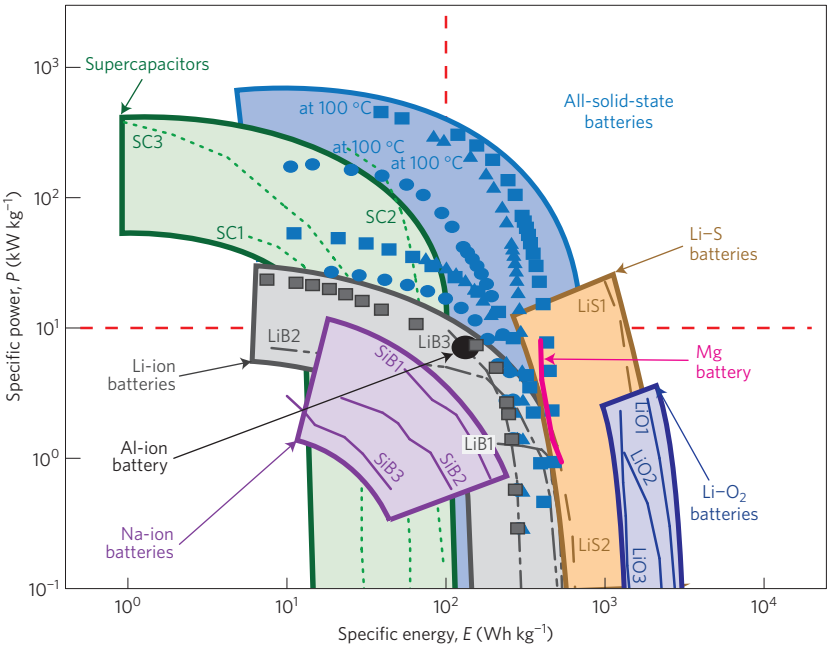

- $Li_4Ti_5O_{12}/LiNbO_3$-coated $LiCoO_2$
- $Li_4Ti_5O_{12}$ + LGPS/LGPS/$LiNbO_3$-coated $LiCoO_2$ + LGPS
- $Li_4Ti_5O_{12}$ + LSiPSCl/LSiPSCl/$LiNbO_3$-coated $LiCoO_2$ + LSiPSCl
- Graphite + LPS/LPS | LGPS/$LiNbO_3$-coated $LiCoO_2$ + LGPS

SC1: activated carbon/activated carbon
SC2: reduced graphene oxide RuO_2/RuO_2-polyaniline
SC3: activated carbon/activated carbon

LiB1: graphite/$LiCoO_2$
LiB2: Li/$LiFePO_4$
LiB3: $Li_4Ti_5O_{12}/LiNi_{0.5}Mn_{1.5}O_4$

SiB1: $Na_3V_2(PO_4)_3$ (NVP)+graphene/NVP+graphene
SiB2: NVP+CNT/NVP+CNT
SiB3: NVP+activated carbon (AC)/NVP+AC
Al-ion battery: Al/graphite
Mg battery: Mg/V_2O_5

LiS1: Li/S (graphene+single-walled CNT)
LiS2: Li/S

LiO1: Li/O_2 (graphene)
LiO2: Li/O_2 (carbon nanofibres)
LiO3: Li/O_2 (carbon nanotubes (CNT))

Figure 6 | The Ragone plot. The Ragone plots of the cells prepared in this study and previously reported batteries and capacitors. The red dashed line indicates the specific energy $E = 10^2$ Wh kg^{-1} and specific power $P = 10$ kW kg^{-1}. The devices powered by liquid electrolytes show the inverse relationship between specific energy and power. The prepared all-solid-state cells simultaneously achieved high energy and power ($E > 10^2$ Wh kg^{-1} and $P > 10$ kW kg^{-1}), which is difficult to achieve for conventional devices.

Methods

Synthesis. The starting materials used for the synthesis of the $Li_{9.6}P_3S_{12}$ solid electrolyte were Li_2S (>99.9% purity, Idemitsu Kosan), P_2S_5 (>99% purity, Sigma Aldrich), and phosphorus (>99% purity, Kojundo Chemical Laboratory). All of the procedures were conducted under an argon atmosphere inside a glove box. All of the reagents were weighed in the appropriate molar ratio and mixed by planetary ball milling for 120 h. The specimens were then pressed into pellets, sealed in a quartz tube at 10 Pa, and heated between 230 °C and 260 °C for 4 h in a furnace. After heating, the tube was slowly cooled to room temperature. The solid electrolyte, $Li_{10}GeP_2S_{12}$, was prepared by sintering Li_2S (>99.9% purity, Nippon Chemical Industrial), P_2S_5 (>99% purity, Sigma Aldrich) and GeS_2 (>99.99% purity, Kojundo Chemical Laboratory) in appropriate molar ratios[8]. In the case of the solid electrolyte $Li_{9.54}Si_{1.74}P_{1.44}S_{11.7}Cl_{0.3}$, Li_2S (>99.9% purity, Nippon Chemical Industrial), P_2S_5 (>99% purity, Sigma Aldrich), SiS_2 (>98% purity, Alfa Aesar) and LiCl (>99.9% purity, Kojundo Chemicals) were mixed in an appropriate molar ratio. The mixture was then placed in a ZrO_2 pot containing a ZrO_2 ball (ϕ10 mm), and the mixture was mechanically milled using the planetary ball milling apparatus at 370 r.p.m. for 40 h. Following the ball milling procedure, the mixture was placed in a quartz tube and heated at 475 °C for 8 h.

Ionic conductivity measurements. Ionic conductivity values were measured by the a.c. impedance method under an argon atmosphere with an applied frequency of 0.1 Hz to 3 MHz, using a Solartron 1260 frequency response analyser. The sample was pressed into a pellet (diameter 5.5–12 mm; thickness 1–2 mm) and heated in a vacuum at the required temperature for each composition (240 °C $\leq T \leq$ 550 °C). Both sides of the pellet were then coated with Au to act as current collectors.

Crystal structure analysis. XRD data were obtained using a high-flux synchrotronic X-ray source at the BL02B2 beamline at SPring-8. The specimen was sealed in a quartz capillary (about 0.3 mm diameter) in a vacuum for the XRD measurements. The neutron diffraction data were obtained using time-of-flight diffractometers: iMATERIA at the Material and Life Science Experimental Facility of the Japan Proton Accelerator Research Complex. In these studies, samples were sealed in a 6-mm-diameter vanadium cell under Ar using an indium ring. Structural parameters were refined using the Z-Rietveld refinement programs[37] and profile parameters were refined using a pseudo-Voigt profile function. Nuclear density distributions were calculated by employing the maximum entropy method (MEM), using crystal structure factors and standard deviations obtained by Rietveld refinement. All of the MEM calculations were performed using the Z-MEM algorithm in the Z-Code software package[38], which employs the conventional Sakata–Sato algorithm with zeroth-order single-pixel approximation[39]. The Z-three-dimensional algorithm was used to generate nuclear density maps of structures[40].

Preparation of the all-solid-state cell. All of the preparation processes were conducted under an argon atmosphere inside a glove box. The cathode of the all-solid-state cell consisted of $LiNbO_3$-coated $LiCoO_2$ powder, a solid electrolyte powder, and acetylene black powder (Denki Kagaku Kogyo). Before preparing the cell, large electrolyte particles were removed using a sieve (10 μm mesh). The $LiNbO_3$ layer was coated onto commercial $LiCoO_2$ powder (Toda Kogyo) using a fluidized bed granulator (MP-01, Powrex)[41]. The $LiNbO_3$-coated $LiCoO_2$, solid electrolyte ($Li_{10}GeP_2S_{12}$ or $Li_{9.54}Si_{1.74}P_{1.44}S_{11.7}Cl_{0.3}$), and acetylene black powders were mixed in a 60:34:6 (wt%) ratio for 5 min using a vortex mixer. The anode consisted of $Li_4Ti_5O_{12}$ (Ishihara Sangyo), a solid electrolyte, and acetylene black powder mixed in a mortar in a 30:60:10 (wt%) ratio. The graphite anode was prepared by mixing graphite powder (Mitsubishi Chemical) and $Li_{9.6}P_3S_{12}$ in a 40:60 (wt%) ratio. The solid electrolyte powders were used as the separator during the preparation process, and the cathode/separator/anode layers were compressed to form a disc-shaped pellet. The all-solid-state cells were prepared by connecting the cathode and anode to stainless-steel current collectors. The diameter of the all-solid-state cell was 11.28 mm (1 cm^2). The thicknesses of the cathode, electrolyte, $Li_4Ti_5O_{12}$ anode, and graphite anode layers were 28, 240, 103 and 29 μm, respectively.

Preparation of the lithium-ion cell. All of the preparation processes were conducted under an argon atmosphere inside a glove box. The lithium-ion cell was carefully prepared using the same electrode materials, volume ratios, and sizes described for the all-solid-state cells. The cathode consisted of $LiNbO_3$-coated $LiCoO_2$ and acetylene black powder mixed in a 90:10 (wt%) ratio, whereas the anode consisted of $Li_4Ti_5O_{12}$ and acetylene black powder mixed in a 75:25 (wt%) ratio. The electrode powder was mixed with polyvinylidene difluoride (PVDF, Kureha) as a binder, and *N*-methyl-2-pyrrolidone (Nacalai Tesque) as the solvent to yield an electrode slurry. The slurries were then cast onto an aluminium sheet, and the solvent was removed by drying at 80 °C under vacuum. The electrode layers were pressed and then punched into a disc shape with a diameter of 11.28 mm. After the cathode layer was placed onto the anode layer (with polypropylene/polyethylene/polypropylene separator, 47% porosity, Ube Industries), 0.5 ml of the liquid organic electrolyte (1 M $LiPF_6$-ethylene carbonate (EC)/diethyl carbonate (DEC) (50:50, *v*/*v*) (Kishida Chemical)) was dropped onto the cell, and the resulting coin-type cell was sealed. The thicknesses of the cathode, separator and anode layers were 27, 25 and 103 μm, respectively.

Charge and discharge measurements. Charge and discharge experiments of the lithium-ion cell and the all-solid-state cells with $Li_4Ti_5O_{12}$ anodes were conducted between 1.0 and 2.6 V at −30–100 ° C. The dependence of the discharge profiles on the rate was measured after the cells were charged at 2.6 V in the constant current charging mode (0.03 mA cm^{-2} (0.045 C) to 2.6 V) and constant voltage charging mode (the cell voltage held constant until the charging current reached 0.001 mA cm^{-2} (0.015 C)). After charging at 2.6 V, the cells were discharged at a constant current from 0.03 to 1,000 mA cm^{-2}(0.045–1,500 C). The cycling characteristics at 25 °C and at 100 °C were examined at a current density of 0.067 mA cm^{-2} (0.1 C) and 12 mA cm^{-2} (18 C), respectively. The electrochemical properties of the cells were determined using a charge–discharge unit (TOSCAT-3100, Toyo System) and a potentio-galvanostat (Solartron 1260). For the all-solid-state cells containing a graphite anode, charge–discharge measurements were conducted according to the conditions for the $Li_4Ti_5O_{12}$ anode, with the exception of the operation voltage, which was varied between 2.5 V and 4.1 V. The specific capacities of the charge–discharge curves were calculated on the basis of the mass of $LiNbO_3$-coated $LiCoO_2$. The specific energy *E* and specific power *P* for the galvanostatic Ragone plots were calculated using the following equations:

$$E = \frac{1}{m}\int_0^T i * V \, dt \quad (1)$$

$$P = \frac{E}{T} \quad (2)$$

where *i*, *V* and *T* are the static current, cell voltage, and discharge time for reaching the cutoff voltages, respectively, and *m* is the mass of the $LiCoO_2$ cathode material. In the present study, *m* was 4.867 mg for all of the electrochemical systems. The other lines in the Ragone plot were prepared on the basis of the mass of the active material of the cathode (working electrode) reported in the literature.

Chronoamperometry measurements. Chronoamperometric measurements were performed as a function of the voltage step. The cells were maintained at 2.6 V for 3 h before the application of the voltage step. The cell voltage was then stepped down to the appropriate voltage between 2.5 and 0.1 V for discharge. All of the procedures were conducted in an Ar atmosphere.

Received 13 October 2015; accepted 15 February 2016; published 21 March 2016

References

1. Armand, M. & Tarascon, J. M. Building better batteries. *Nature* **451**, 652–657 (2008).
2. Simon, P. & Gogotsi, Y. Materials for electrochemical capacitors. *Nature Mater.* **7**, 845–854 (2008).
3. Scrosati, B. & Garche, J. Lithium batteries: status, prospects and future. *J. Power Sources* **195**, 2419–2430 (2010).
4. Goodenough, J. Rechargeable batteries: challenges old and new. *J. Solid State Electrochem.* **16**, 2019–2029 (2012).
5. Winter, M. & Brodd, R. J. What are batteries, fuel cells, and supercapacitors? *Chem. Rev.* **104**, 4245–4269 (2004).
6. Robinson, A. L. & Janek, J. Solid-state batteries enter EV fray. *MRS Bull.* **39**, 1046–1047 (2014).
7. Seino, Y. *et al.* A sulphide lithium super ion conductor is superior to liquid ion conductors for use in rechargeable batteries. *Energy Environ. Sci.* **7**, 627–631 (2014).
8. Kamaya, N. *et al.* A lithium superionic conductor. *Nature Mater.* **10**, 682–686 (2011).
9. Wang, Y. *et al.* Design principles for solid-state lithium superionic conductors. *Nature Mater.* **14**, 1026-1031 (2015).
10. Ohtomo, T. *et al.* All-solid-state lithium secondary batteries using the $75Li_2S{\cdot}25P_2S_5$ glass and the $70Li_2S{\cdot}30P_2S_5$ glass-ceramic as solid electrolytes. *J. Power Sources* **233**, 231–235 (2013).
11. Kwon, O. *et al.* Synthesis, structure, and conduction mechanism of the lithium superionic conductor $Li_{10+\delta}Ge_{1+\delta}P_{2-\delta}S_{12}$. *J. Mater. Chem. A* **3**, 438–446 (2015).
12. Hori, S. *et al.* Structure–property relationships in lithium superionic conductors having a $Li_{10}GeP_2S_{12}$-type structure. *Acta Crystallogr. B* **B71**, 727–736 (2015).
13. Kanno, R. *et al.* A self-assembled breathing interface for all-solid-state ceramic lithium batteries. *Electrochem. Solid-State Lett.* **7**, A455-A458 (2004).

14. Bron, P. *et al.* $Li_{10}SnP_2S_{12}$: an affordable lithium superionic conductor. *J. Am. Chem. Soc.* **135**, 15694–15697 (2013).
15. Kuhn, A. *et al.* A new ultrafast superionic Li-conductor: ion dynamics in $Li_{11}Si_2PS_{12}$ and comparison with other tetragonal LGPS-type electrolytes. *Phys. Chem. Chem. Phys.* **16**, 14669–14674 (2014).
16. Hori, S. *et al.* Synthesis, structure, and ionic conductivity of solid solution, $Li_{10+\delta}M_{1+\delta}P_{2-\delta}S_{12}$ (M = Si, Sn). *Faraday Discuss.* **176**, 83–94 (2014).
17. Huang, W. & Frech, R. Vibrational spectroscopic and electrochemical studies of the low and high temperature phases of $LiCo_{1-x}M_xO_2$ (M = Ni or Ti). *Solid State Ion.* **86–88**, 395–400 (1996).
18. Ohta, S., Kobayashi, T., Seki, J. & Asaoka, T. Electrochemical performance of an all-solid-state lithium ion battery with garnet-type oxide electrolyte. *J. Power Sources* **202**, 332–335 (2012).
19. Aoki, K., Baars, A., Jaworski, A. & Osteryoung, J. Chronoamperometry of strong acids without supporting electrolyte. *J. Electroanal. Chem.* **472**, 1–6 (1999).
20. Wetjen, M., Kim, G.-T., Joost, M., Winter, M. & Passerini, S. Temperature dependence of electrochemical properties of cross-linked poly(ethylene oxide)–lithium bis(trifluoromethanesulfonyl)imide–N-butyl-N-methylpyrrolidinium bis (trifluoromethanesulfonyl) imide solid polymer electrolytes for lithium batteries. *Electrochim. Acta* **87**, 779–787 (2013).
21. Capiglia, C. *et al.* ^{7}Li and ^{19}F diffusion coefficients and thermal properties of non-aqueous electrolyte solutions for rechargeable lithium batteries. *J. Power Sources* **81–82**, 859–862 (1999).
22. Abe, T., Fukuda, H., Iriyama, Y. & Ogumi, Z. Solvated Li-ion transfer at interface between graphite and electrolyte. *J. Electrochem. Soc.* **151**, A1120–A1123 (2004).
23. Abe, T., Sagane, F., Ohtsuka, M., Iriyama, Y. & Ogumi, Z. Lithium-ion transfer at the interface between lithium-ion conductive ceramic electrolyte and liquid electrolyte—A key to enhancing the rate capability of lithium-ion batteries. *J. Electrochem. Soc.* **152**, A2151–A2154 (2005).
24. Choi, D. *et al.* Li-ion batteries from $LiFePO_4$ cathode and anatase/graphene composite anode for stationary energy storage. *Electrochem. Commun.* **12**, 378–381 (2010).
25. Lee, S. W. *et al.* High-power lithium batteries from functionalized carbon-nanotube electrodes. *Nature Nanotech.* **5**, 531–537 (2010).
26. Nagasubramanian, G. Electrical characteristics of 18650 Li-ion cells at low temperatures. *J. Appl. Electrochem.* **31**, 99–104 (2001).
27. Cericola, D., Novák, P., Wokaun, A. & Köttz, R. Hybridization of electrochemical capacitors and rechargeable batteries: an experimental analysis of the different possible approaches utilizing activated carbon, $Li_4Ti_5O_{12}$ and $LiMn_2O_4$. *J. Power Sources* **196**, 10305–10313 (2011).
28. Khomenko, V., Raymundo-Piñero, E. & Béguin, F. A new type of high energy asymmetric capacitor with nanoporous carbon electrodes in aqueous electrolyte. *J. Power Sources* **195**, 4234–4241 (2010).
29. Zhang, J., Jiang, J., Li, H. & Zhao, X. S. A high-performance asymmetric supercapacitor fabricated with graphene-based electrodes. *Energy Environ. Sci.* **4**, 4009–4015 (2011).
30. Gallant, B. M. *et al. The Lithium Air Battery* 121–158 (Springer, 2014).
31. Peng, H.-J. *et al.* Nanoarchitectured graphene/CNT@porous carbon with extraordinary electrical conductivity and interconnected micro/mesopores for lithium-sulfur batteries. *Adv. Funct. Mater.* **24**, 2772–2781 (2014).
32. Imamura, D., Miyama, M., Hibino, M. & Kubo, T. Mg intercalation properties into V_2O_5 gel/carbon composites under high-rate condition. *J. Electrochem. Soc.* **150**, A753–A758 (2003).
33. Lin, M.-C. *et al.* An ultrafast rechargeable aluminium-ion battery. *Nature* **520**, 324–328 (2015).
34. Li, S. *et al.* Effect of carbon matrix dimensions on the electrochemical properties of $Na_3V_2(PO_4)_3$ nanograins for high-performance symmetric sodium-ion batteries. *Adv. Mater.* **26**, 3545–3553 (2014).
35. Ohta, N. *et al.* Enhancement of the high-rate capability of solid-state lithium batteries by nanoscale interfacial modification. *Adv. Mater.* **18**, 2226–2229 (2006).
36. Maier, J. Nanoionics: ion transport and electrochemical storage in confined systems. *Nature Mater.* **4**, 806–815 (2005).
37. Oishi, R. *et al.* Rietveld analysis software for J-PARC. *Nucl. Instrum. Methods Phys. Res. A* **600**, 94–96 (2009).
38. Ishikawa, Y. *et al.* Z-MEM & Z-3D, maximum entropy method and visualization software for electron/nuclear density distribution in Z-Code. In *ICANS XXI* DAA-P08 (J-PARC, 2014).
39. Sakata, M. & Sato, M. Accurate structure analysis by the maximum-entropy method. *Acta Crystallogr. A* **46**, 263–270 (1990).
40. Ishikawa, Y., Yonemura, M. & Kamiyama, T. *Z-3D, Textbook of Z-code Powder Diffraction Data Analysis School* (KEK, 2014).
41. Ohta, N. *et al.* $LiNbO_3$-coated $LiCoO_2$ as cathode material for all solid-state lithium secondary batteries. *Electrochem. Commun.* **9**, 1486–1490 (2007).

Acknowledgements

The authors thank T. Yabutani, R. Saito and K. Mukoyama for their support in the preparation of the all-solid-state and lithium-ion cells. They also thank H. Hirokawa for his support in the synthesis of $Li_{9.6}P_3S_{12}$. This study was supported by the Post-LiEAD project of the New Energy and Industry Technology Development Organization (NEDO), Japan. The synchrotron radiation experiments were carried out as projects approved by the Japan Synchrotron Radiation Institute (JASRI) (proposal No. 2014A1408 and 2014A1763). The neutron radiation experiments were performed at the Japan Proton Accelerator Research Complex (J-PARC) (proposal No. 2014AM1004, 2014BM0006 and 2014BM0012).

Author contributions

Y.K. and S.H. designed and conducted the experimental work. Y.K., S.H., T.S., K.S., M.H. and R.K. analysed the electrochemical data. S.H., A.M. and M.Y. measured the synchrotron X-ray and neutron diffraction of superionic conductors. Y.K., S.H., M.Y. and R.K. analysed the crystal structure. Y.K., S.H. and R.K. wrote the manuscript. H.I. and R.K. directed this work.

Additional information

Supplementary information is available online. Reprints and permissions information is available online at www.nature.com/reprints. Correspondence and requests for materials should be addressed to Y.K. or R.K.

Competing interests

The authors declare no competing financial interests.